Gyrokinetic Simulations of Energetic Particle-Driven TAE/EPM Transport Embedded in ITG/TEM Microturbulence

E.M. Bass and R.E. Waltz

General Atomics, P.O. Box 85608, San Diego, California 92186-5608

e-mail: bassem@fusion.gat.com

Abstract. Energetic particle (EP) transport from local high-n toroidal Alfvén eigenmodes (TAEs) and energetic particle modes (EPMs) is simulated with a gyrokinetic code. The TAE and EPM are found unstable alongside the well-known ion-temperature-gradient (ITG) and trapped-electron-mode (TEM) instabilities. Nonlinearly saturated states of local TAE/EPM turbulent intensity show a "soft" transport threshold for enhanced EP transport against the TAE/EPM-driving EP pressure gradient. The meso-scale TAE/EPM transport saturates by nonlinear interaction with microturbulent ITG/TEM-driven zonal flows. Such saturated states with fixed driving gradients are accessible only within a narrow range of EP drive above the TAE/EPM linear instability threshold. Above a critical EP pressure gradient, EP transport is unbounded in the simulations, which do not include limitations of the EP source. If background plasma gradients driving the ITG/TEM turbulence and zonal flows are weakened, this critical gradient collapses to the TAE/EPM linear stability threshold and the soft transport regime vanishes. Background species transport appears to be largely unaffected in all regimes.

1. Introduction

In many modern fusion experiments (e.g. [1–5]), a heating beam destabilizes low-n Alfvén eigenmodes such as the toroidal Alfvén eigenmode (TAE) [6–9], the energetic particle mode (EPM) [10], and the reverse shear Alfvén eigenmode (RSAE) [11,12] among others. Similar instabilities expected at higher n in future fusion experiments and reactors are driven by fusion alpha particles. In either case, a radial pressure gradient in the energetic particle (EP) population provides the free energy that powers finite-n instabilities. An accessible review of experiment is available in Ref. [13]. See Refs. [14] and [15] and references therein for a detailed review of Alfvén eigenmode stability.

In this paper, we focus on the burning plasma scenario where the EPs are fusion-produced alpha particles. The work here differs in approach from many previous analyses. The more common global, hybrid kinetic-magnetohydrodynamic (MHD) treatment [16–20] follows gyrokinetic EPs in the presence of global Alfvén eigenmodes in a thermal MHD plasma. We treat all species (thermal and EP) gyrokinetically with the GYRO code [21,22]. Looking to the limit of a large, high-field machine (ion gyroradius small compared to machine radius), we restrict our analysis to local simulations with fixed driving gradients. Usual self-saturation mechanisms such as particle trapping and flattening of the EP pressure profile [23,24] — referred to here as "quasilinear" saturation — are precluded in these simulations. Without profile relaxation (phase space-local or otherwise), the only saturation mechanism available is nonlinear interaction of finite-n fluctuations and $n=0$ zonal flows.

GYRO has investigated local and global drift-wave microturbulence and transport from moderately long-wave ion temperature gradient (ITG) and trapped electron mode (TEM) instabilities (for a review to 2004 see Ref. [25]) as well as very short wave electron temperature gradient (ETG) instabilities [26]. Convective transport of EPs (at the trace level) by electrostatic ITG/TEM was found in GYRO [27] to diminish with increasing EP energy, consistent with subsequent results in a stochastic test field [28] and a quasilinear, gyrokinetic transport model [29]. Similar results have been recovered in the gyrokinetic codes GTC [30] and GENE [31]. We apply the same techniques as in Ref. [27] here, but include very long-wave Alfvén eigenmodes, driven unstable by the EPs, alongside ITG/TEM microturbulence.

We explore under what conditions fixed-gradient nonlinearly saturated states exist or when such states give way to unbounded EP transport and relaxation of the EP pressure gradient.

2. Simulation Parameters

In most of the present simulations, both linear and nonlinear, background plasma parameters are given by the well-studied GA-standard case [32,33]. This corresponds to a deuterium plasma in axisymmetric, large aspect ratio circular geometry "$s-\alpha$ model" (with $\alpha=0$) [34] with temperature $T_i = T_e$, safety factor $q=2$ at the center of the simulation domain, and shear $\hat{s} = d\ln q/d\ln r = 1$. Finite-aspect-ratio particle trapping is included. The toroidal major radius $R/a=3$, and simulations always center on minor radius $r/a=0.5$. Here, a is the plasma minor radius. The ion and electron temperature and density gradients are given by $a/L_{T_e} = a/L_{T_i} = 3$ and $a/L_{n_e} = a/L_{n_i} = 1$, where $L_f \equiv -f(\partial f/\partial r)^{-1}$ is the radial gradient length of equilibrium quantity *f*. All equilibrium quantities are constant or vary linearly across the radial domain (flux-tube model). The ratio of electron pressure to magnetic pressure $\beta_e = 0.002$.

A sparse population of energetic alpha particles with a radial density gradient is added to destabilize Alfvén modes. Radial gradient lengths are held fixed at $a/L_{n_{EP}} = 4$ and $a/L_{T_{EP}} = 0$, where the subscript EP denotes the sparse energetic particle population. The EPs are Maxwellian in velocity space with temperature $T_{EP} = 100\,T_e$, roughly in accordance with the equivalent temperature of a slowing-down distribution of alpha particles in a typical burning plasma fusion experiment [27].

The Alfvén drive strength from the EP pressure gradient $\left[(n_{EP}/n_e)(T_{EP}/T_e)(R/L_{n_{EP}})\right]$ is varied through the relative energetic particle density n_{EP}/n_e in the range $0.1\% \le n_{EP}/n_e \le 3.5\%$. Note Table III in Ref. [27] suggests the classical slowing down alpha density will be less than 1%. The deuterium ion density n_i (charge *e*) is varied with energetic alpha particle n_{EP} (charge 2*e*) to keep the equilibrium plasma charge neutral: $n_i + 2n_{EP} = n_e$. Care is needed to choose parameters that drive the TAE/EPM modes unstable while staying below the high-*n* MHD beta limits. For the GA-standard case parameters with $\beta_e = 0.002$, the projected linear MHD high-*n* ballooning mode stability threshold, including EP pressure, is reached when $n_{EP}/n_e = 5.2\%$. In the absence of $E\times B$ shear, a nonlinear MHD sub-critical gradient, after which nonlinear simulations fail to saturate due to radial density oscillations [35], is projected when $n_{EP}/n_e = 1.0\%$.

Neglecting electron mass, the Alfvén velocity v_A in the simulations is given by: $v_A = B/\sqrt{4\pi(n_i m_i + n_{EP} m_{EP})}$. Since the energetic alpha particles have $m_{EP} = 2m_i$, $v_A/c_s = \sqrt{2/\beta_e} = 31.6$ at $\beta_e = 0.002$ in GYRO-preferred units. The sound speed is given by $c_s = \sqrt{T_e/m_i}$. Note that the physical choice of energetic particle temperature $T_{EP} = 100\,T_e$ gives an EP thermal speed of $v_{thEP} = \sqrt{2T_{EP}/m_{EP}} = 10c_s$. Unstable TAEs and EPMs are seen at an EP density around $n_{EP}/n_e = 0.5\%$.

3. Linear Simulations

Unless otherwise noted, all linear simulations were performed in the GYRO thin-flux-tube model. The velocity-space grid has 128 points (8 energy, 8 pitch angles, 2 parallel velocity directions). Simulated energies lie in the range $0 < \varepsilon_\sigma \le 5$, where $\varepsilon_\sigma = E_\sigma/T_\sigma$ is the rescaled kinetic energy E_σ for each species σ. The pitch-angle grid includes 4 points each in the trapped and passing ranges. In real space, the grid has 10 points along the field line and 6 points along the radial direction. Domain width $L_{x,n}$ perpendicular to the central flux surface (at $r_0/a = 0.5$) varies with the toroidal mode number *n* considered according to $L_{x,n} = r_0/(nq\hat{s})$, the distance between two singular surfaces. Here *x* is the radius-like flux

surface label, identical to radius in the $s-\alpha$ model. Perturbations obey periodic radial boundary conditions, precluding flattening across the radial domain.

In addition to solutions of the initial-value problem, we present spectral results from an eigenvalue solver recently implemented in GYRO. The solver uses public SLEPc [36] eigenvalue libraries, based on PETSc [37–39] linear solvers. In each case, frequency and growth rate of the leading modes are given by the eigenvalues of a matrix corresponding to the linear problem. For the grid dimensions above, each matrix is 23040×23040 (128×10×6×3 kinetic species). A similar solver has been implemented in the GENE code [40].

Instead of toroidal mode number n, it is convenient instead to refer to the dimensionless normalized wavenumber $k_\theta\rho_s = (nq/r)\rho_s$. Here $\rho_s = c_s/\Omega_i$ is the ion sound Larmor radius and $\Omega_i = eB/m_ic$ is the ion cyclotron frequency. The local gyrokinetic equations depend on n only through this parameter, and adjusting $\rho_* = \rho_s/a$ is equivalent to changing n. However, $\rho_* = 0.0025$ (used in most cases displayed in this paper) corresponds to a mid-radius value in a typical 2 Tesla DIII-D L-mode discharge, so that $k_\theta\rho_s = 0.05$ corresponds to $n = 5$. In ITER, ρ_* (n) will be 3–5 fold smaller (larger).

A linear eigenvalue scan in $k_\theta\rho_s$ at $n_{EP}/n_e = 2.5\%$ shows two EP-driven peaks in growth rate [Fig. 1(a)] at values of $k_\theta\rho_s$ well below $k_\theta\rho_{EP} = 1$, where $\rho_{EP} = 5\sqrt{2}\rho_i = 10\rho_s$ is the energetic particle Larmor radius. The frequency of the first-peak mode is proportional to $k_\theta\rho_s$ [Fig. 1(b)] at low values of $k_\theta\rho_s$. Throughout the paper, the ion diamagnetic frequency direction is indicated by $\omega > 0$. The frequency of the second-peak mode moves into the TAE continuum gap, bounded by frequencies $\omega_\pm = \omega_{TAE}/\sqrt{1 \mp 2(r/R)}$ [8], as $k_\theta\rho_s$ is increased. Here $\omega_{TAE} = v_A/2qR$ is the TAE frequency. The mode most closely resembles a canonical TAE, approaching a constant frequency within the continuum gap, in this range. The first-peak mode has a frequency below the TAE gap boundary throughout its unstable range. We label the modes associated with the first and second EP-driven peaks the EPM and TAE respectively.

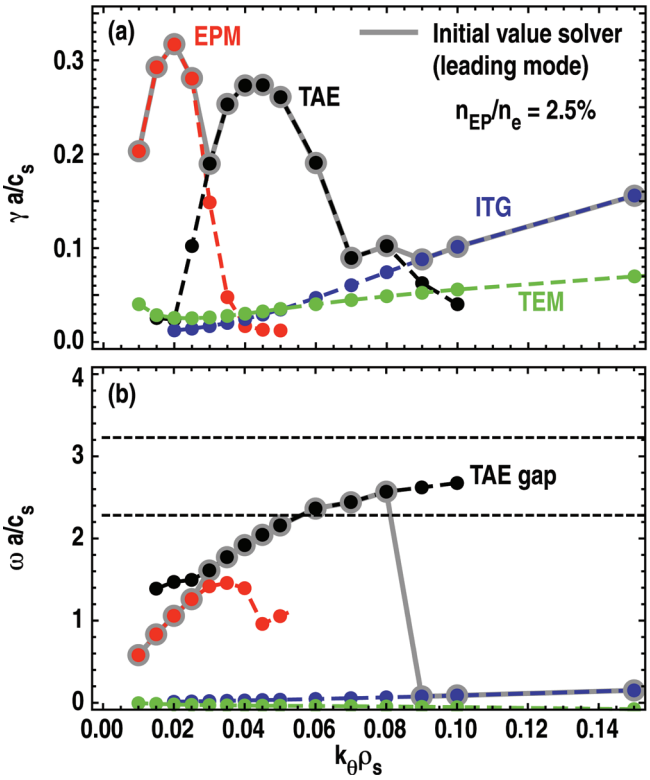

FIG. 1. Growth rate (a) and frequency (b) vs. $k_\theta\rho_s$ for the four most unstable modes in a thin flux tube at $n_{EP}/n_e = 2.5\%$. Eigenvalue solver (colored curves) and initial value (gray curves) results are shown. TAE/EPM instabilities are confined to $k_\theta\rho_{EP} < 1$ ($k_\theta\rho_s < 0.14$). The ITG growth-rate peak of $\gamma\, a/c_s = 0.21$ at $k_\theta\rho_s = 0.3$ is not shown.

At the energetic particle drive level $n_{EP}/n_e = 2.5\%$ shown in Fig. 1(a), the EPM and TAE growth rate peak at $\gamma\, a/c_s = 0.31$ and $\gamma\, a/c_s = 0.27$ respectively. The peak ITG growth rate of $\gamma\, a/c_s = 0.21$ occurs at $k_\theta\rho_s = 0.3$ (not shown). The TEM linear growth rate increases monotonically, taking the value $\gamma\, a/c_s = 0.16$ at $k_\theta\rho_s = 0.75$ near the edge of the considered range. At the sub-critical β limit $n_{EP}/n_e = 1.0\%$, ITG/TEM components are relatively unchanged, but the TAE/EPM growth-rate peaks are less pro-

nounced than in Fig. 1(a). The maximum growth rates of the EPM and TAE are reduced to $\gamma a/c_s = 0.053$ and $\gamma a/c_s = 0.068$, respectively.

4. Nonlinear Transport Simulations

All nonlinear simulations reported here track 40 interacting modes covering the range $0 \le k_\theta \rho_s \le 0.78$ spaced $\Delta(k_\theta \rho_s) = 0.02$ apart, corresponding to mode number spacing $\Delta n = 2$ (half-torus simulation) at the simulated value $\rho_* = 0.0025$. This range of $k_\theta \rho_s$ includes most medium-$k_\theta \rho_s$ ITG/TEM fluctuations in addition to the low-$k_\theta \rho_s$ TAE/EPM, but excludes the high-$k_\theta \rho_s$ ETG. A well-converged ITG/TEM simulation would only require a mode spacing of $\Delta n = 5$ (i.e. 16 modes). Resolution of low-$k_\theta \rho_s$ TAE/EPM requires the unusually high mode density used here.

The radial domain width L_x is chosen to equal the poloidal extent of one cycle of the longest-wavelength ($n = 2$) mode at the center of the simulation domain ($r = 0.5a$): $L_x = 2\pi/(nq/r) = \pi a/4 = 314\rho_s$. This gives a square simulation domain perpendicular to the magnetic field that appears to accommodate the largest eddies observed. The simulation box lengths are about 3-fold larger than normally used for the GA-std ITG/TEM case. There are 425 radial grid points spaced $\delta x = 0.75\rho_s$ apart. All other grid dimensions and simulation parameters are the same as in the linear simulations of Sec. 3. The perturbation follows periodic radial boundary conditions, excluding all profile-flattening effects. Note that the condition $L_x \propto 1/n_{\min}$ implies that an ITG/TEM-only simulation requires much less radial extent. In this way, increased box lengths required for TAE/EPM simulations doubly impacts simulation cost. Including reduced time step, longer box lengths, expensive (50 point in place of 15 point) gyro-averaging for energetic particles, and longer run times to accommodate the slow TAE/EPM growth rates, TAE/EPM-inclusive nonlinear simulations require more than 100 times more computing resources than their ITG/TEM-only counterpart.

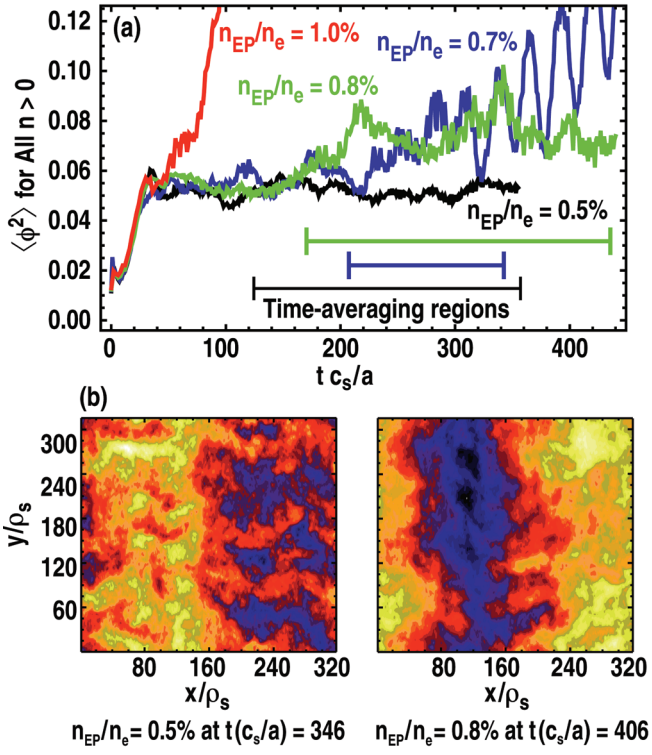

FIG. 2. The sum of finite-n potential fluctuations [$\hat{\phi} = (e\delta\phi/T_e)$] in four local, 40-mode, nonlinear simulations (a). Saturation is seen below the TAE/EPM nonlinear drive threshold (n_{EP}/n_e = 0.5%, black curve) and in the "soft-onset" TAE/EPM-driven region ($n_{EP}/n_e = 0.8\%$, green curve). The unbounded transport region shows rapid runaway ($n_{EP}/n_e = 1.0\%$, red curve). Anomalous, slow runaway is sometimes seen in the soft-onset region ($n_{EP}/n_e = 0.7\%$, blue curve). Potential fluctuations in the two saturated cases (b) show increased eddy size with TAE/EPM onset. Peaks are yellow and troughs are blue or black.

Below the TAE/EPM stability threshold, the EPs are tracers convected by ITG/TEM turbulence. Finite TAE/EPM fluctuation intensity appears near $n_{EP}/n_e = 0.5\%$. At or below this drive strength, EP transport closely resembles electrostatic EP transport previously observed in GYRO [27]. Above this threshold, the saturated TAE/EPM turbulent intensity increases gradually with n_{EP}/n_e. No saturated states were

observed above $n_{EP}/n_e = 0.8\%$; this is close to the sub-critical β limit at $n_{EP}/n_e = 1.0\%$ but we believe this is not the cause. Some simulations in the range $0.5\% < n_{EP}/n_e < 0.8\%$ also failed to saturate, exhibiting a slow runaway at long times. Figure 2(a) shows the finite-$k_\theta\rho_s$ potential fluctuations for some representative cases. In all runaway cases, the lowest-wavenumber mode at $k_\theta\rho_s = 0.02$, dominates the spectrum.

Figure 2(b) shows snapshots of the electrostatic potential ϕ in the plane perpendicular to the magnetic field for the two saturated cases in Fig. 2(a) ($n_{EP}/n_e = 0.5\%$ and $n_{EP}/n_e = 0.8\%$). As previously indicated, x is the radial coordinate running perpendicular to the flux surface. The angular y coordinate runs perpendicular to the magnetic field but within the flux surface. At $n_{EP}/n_e = 0.5\%$ [Fig. 2(a), black curve and 2(b), left], eddy structure reflects ITG/TEM activity only. As TAE/EPM drive increases to $n_{EP}/n_e = 0.8\%$ [Fig. 2(a), green curve and 2(b), right), increased eddy size reflects low-$k_\theta\rho_s$ activity. The larger structures in the right side of Fig. 2(b) are well separated in the radial coordinate x, but less clearly so in the perpendicular poloidal coordinate y. Slow runaway below $n_{EP}/n_e = 0.8\%$ may be influenced by periodic eddies reinforcing themselves in the y direction. A future (expensive) simulation with greater mode resolution ($\Delta n = 2 \rightarrow \Delta n = 1$, 40 modes→80 modes), corresponding to an increased effective y domain length, may resolve the issue.

Figure 3 shows the $k_\theta\rho_s$-spectrum of potential intensity for the two saturated cases in Fig. 2(a) averaged over the time periods shown in the same figure. In the $n_{EP}/n_e = 0.5\%$ case (Fig. 3, black bars), where EP drive is insufficient to drive significant TAE/EPM fluctuations, the spectrum shows predominantly ITG/TEM activity. In the driven $n_{EP}/n_e = 0.8\%$ case (Fig. 3, green, crosshatched bars), TAE/EPM fluctuations at low $k_\theta\rho_s$ strongly appear. Increased shear at low $k_\theta\rho_s$ also modestly reduces the higher-$k_\theta\rho_s$ ITG/TEM fluctuation intensity.

In creating background species turbulent transport, ITG/TEM fluctuations generate most of the sheared zonal flows needed for EP transport saturation. Our simulations fail to saturate when this ITG/TEM turbulence and transport is sufficiently reduced. Figure 4 shows the total finite-$k_\theta\rho_s$ potential of three such cases. The saturated $n_{EP}/n_e = 0.8\%$ case from Fig. 2(a) (green curve) is shown for comparison. All cases in Fig. 4 have the same EP kinetic drive. ITG/TEM transport has been reduced in the

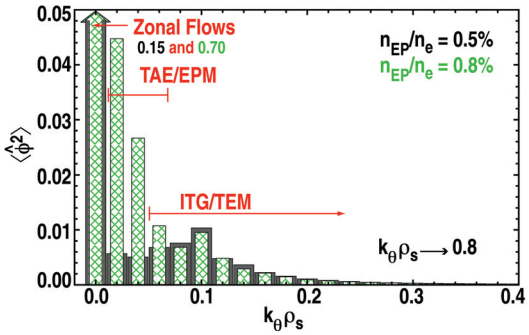

FIG. 3. The $k_\theta\rho_s$ spectrum of potential fluctuations for the EP-tracer (n_{EP}/n_e = (0.5%, black bars) and soft-onset TAE/EPM-driven ($n_{EP}/n_e = 0.8\%$, green, crosshatched bars) regimes. The simulated spectrum extends to $k_\theta\rho_s = 0.8$ (not shown).

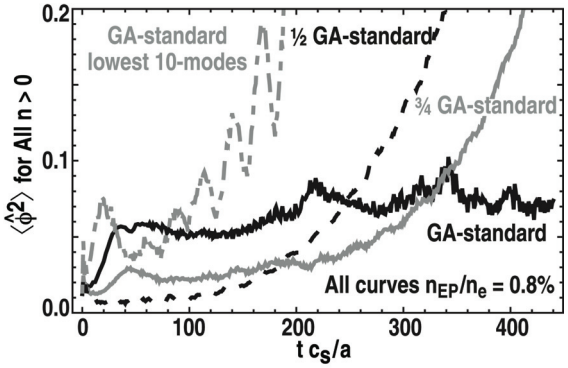

FIG. 4. Time trace of finite-n, normalized fluctuation intensity [$\hat{\phi} = (e\delta\phi/T_e)$] at n_{EP}/n_e = 0.8% in four nonlinear simulations with varying levels of background ITG/TEM turbulence. The GA-standard case (black curve) shows soft TAE/EPM onset. Reducing ITG/TEM fluctuations — by lowering background gradients (three-quarters GA-standard, gray curve or one-half GA-standard, black-dashed curve) or keeping only the lowest 10 modes (gray, dot-dashed curve) — ITG/TEM drive is insufficient for zonal-flow-mediated soft TAE/EPM onset.

runaway cases by two different methods: background gradient reduction and spectral clipping. The gray curve shows gradients at three-fourths of the GA-standard values ($a/L_{T_e} = a/L_{T_i} = 2.25$ and $a/L_{n_e} = a/L_{n_i} = 0.75$). The black, dashed line shows background species gradients turned down to half the GA-standard values ($a/L_{T_e} = a/L_{T_i} = 1.5$ and $a/L_{n_e} = a/L_{n_i} = 0.5$). The third case (gray, dot-dashed curve, Fig. 4) shows a lowest 10-mode simulation covering the range $0 \le k_\theta \rho_s \le 0.18$. Mode density and radial domain are the same as all other nonlinear simulations. Here, much of the ITG/TEM spectrum is cut out with its accompanying transport. Again zonal-flow generation is insufficient for saturation.

Figure 5 shows the contribution per mode to the EP density diffusion coefficient D_{EP}, normalized to the gyroBohm diffusivity $\chi_{gB} = (c_s/a)\rho_s^2$, for two cases averaged over the time periods shown in Fig. 2(a). See Ref. [21] for details of how transport coefficients are obtained in GYRO. In the absence of TAE/EPM activity ($n_{EP}/n_e = 0.5\%$, black bars), transport comes primarily from the ITG/TEM length scales. Above the TAE/EPM drive threshold ($n_{EP}/n_e = 0.8\%$, green, crosshatched bars), a roughly 30% enhancement comes entirely from low-$k_\theta\rho_s$ TAE/EPM activity. Reduced ITG/TEM fluctuations from low-$k_\theta\rho_s$ shear (Fig. 3) account for the slight decrease in ITG/TEM transport in the latter case.

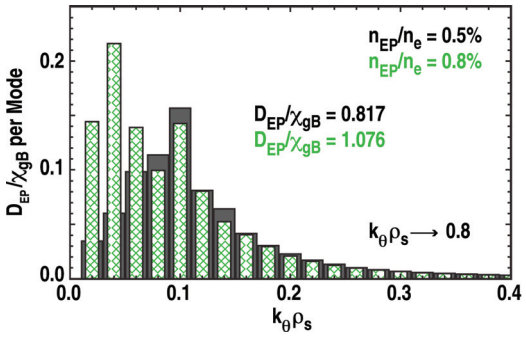

FIG. 5. Contribution per mode to the energetic particle diffusion coefficient D_{EP} for an EP-tracer case ($n_{EP}/n_e = 0.5\%$, black bars) and a TAE/EPM-driven case in the soft-onset regime ($n_{EP}/n_e = 0.8\%$, green, crosshatched bars). The simulated spectrum extends to $k_\theta\rho_s = 0.8$ (not shown).

The transport fluxes include contributions from both $E \times B$ and magnetic flutter transport. In general, we find that the magnetic flutter contribution remains below 20% of the total energy or particle flux, across the $k_\theta\rho_s$ spectrum. For the driven $n_{EP}/n_e = 0.8\%$ case (Fig. 5, green, crosshatched bars), magnetic flutter accounts for about 11% of the total EP particle flux. When only the three lowest $k_\theta\rho_s$ modes are considered, accounting for the bulk of TAE/EPM induced transport, the magnetic flutter contribution increases to about 15%. $E \times B$ flux dominates both ITG/TEM and TAE/EPM EP particle transport.

The EP density diffusion coefficient D_{EP} is plotted against the drive strength parameter n_{EP}/n_e in Fig. 6. Above $n_{EP}/n_e = 0.5\%$, where the TAE/EPM growth rates exceed the low-$k_\theta\rho_s$ ITG/TEM growth rate, the onset of TAE/EPM fluctuations in the turbulent spectrum produces gradually increasing EP particle transport. The effective stiffness S in the driven region is given by $S \equiv 1 + \partial \ln D_{EP} / \partial \ln(n_{EP}/n_e) \cong 1.5$. By comparison, core ITG/TEM energy transport near the ITG threshold can

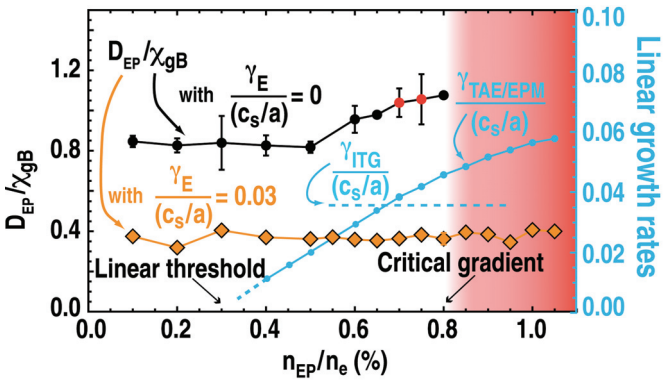

FIG. 6. The normalized EP diffusion coefficient D_{EP} vs. TAE/EPM drive strength n_{EP}/n_e. The shear-free transport (black curve) increases slowly (stiffness $S \approx 1.5$) with drive until the critical gradient. Low $E \times B$ shear ($\gamma_E a/c_s = 0.03$, orange line) suppresses TAE/EPM transport in the range shown. Red dots show cases of anomalous, slow runaway at long times. The leading Alfvén growth rate (blue curve, right axis) is shown for reference.

have stiffness (with respect to ion temperature gradient) exceeding 7 (Fig. 8, Ref. [41]). The runaway region (marked in red in Fig. 6) starts above $n_{EP}/n_e = 0.8\%$ and suggests the normalized critical EP pressure gradient $[(n_{EP}/n_e)(T_{EP}/T_e)(R/L_{nEP})] \sim 1$. The unsheared linear growth rate of the ITG mode and leading high-frequency mode at $k_\theta \rho_s = 0.05$ are shown in Fig. 6 for reference. Note the relative locations of the *linear threshold gradient* (at $n_{EP}/n_e \approx 0.3\%$) and the runaway transport *critical gradient* (at $n_{EP}/n_e = 0.8\%$). The TAE/EPM "soft-onset" *narrow range* exists between these two points.

Low-$k_\theta \rho_s$ TAE/EPM transport contributions (first green peak in Fig. 5) are easily suppressed by $E \times B$ flow shear. A modest shearing rate of $\gamma_E \equiv (r/q)\partial[(cq/rB)\partial\Phi_0/\partial r]/\partial r = 0.03\,(c_s/a)$, half the largest TAE/EPM linear growth rate at $n_{EP}/n_e = 1.0\%$, eliminates TAE/EPM transport enhancement across all drive strengths tested (orange line, Fig. 6). At this level of shearing, EP transport from ITG/TEM turbulence drops to about half its unsheared level.

5. Summary

The simulations discussed here show that fixed-gradient, nonlinearly saturated states of longwave TAE/EPM turbulent transport can be found within a *narrow range* of EP pressure-gradient drive between the TAE/EPM *linear threshold gradient* and a significantly (approximately 2-fold) higher *critical gradient*, provided the background ITG/TEM turbulence is sufficiently large. In this case, $E \times B$ shear from ITG/TEM-driven $n = 0$ zonal flows is then large enough to nonlinearly saturate the longwave TAE/EPM-EP transport. A moderate (up to 30%) EP transport enhancement from TAE/EPM activity has a "soft turn-on" as the EP pressure gradient is increased within a *narrow range* up to the *critical gradient*. For EP pressure gradients beyond the *critical gradient,* fixed-gradient nonlinearly saturated states apparently do not exist.

In a physical system, EP radial transport flow is limited by the source rates and we expect the EP pressure gradient profile would relax back to the *critical gradient* as EP transport tried to run away. Crucially, we find that the *narrow range* vanishes (the *critical gradient* becomes the *linear threshold gradient*) when ITG/TEM transport is sufficiently reduced, leading to stiff TAE/EPM transport of EPs.

This work was supported by the US Department of Energy under DE-FG02-95ER54309. The authors gratefully acknowledge Ming Chu for productive discussions, ideas, and assistance, particularly in the early stages of this project. Thanks also to Jeff Candy and Guoyong Fu for illuminating discussions.

References

[1] SHINOHARA, K., *et al.,* Nucl. Fusion **41** (2001) 603
[2] VAN ZEELAND, M.A., *et al.,* Plasma Phys. Control. Fusion **47** (2005) L31
[3] FREDRICKSON, E.D., *et al.,* Phys. Plasmas **13**(2006) 056109
[4] GÜNTER, S., *et al.,* Nucl. Fusion **47** (2007) 920
[5] NAZIKIAN, R., *et al.,* Phys. Plasmas **16** (2009) 056107
[6] CHENG, C.Z., *et al.,* Phys. Fluids **29** (1986) 695
[8] FU, G.Y. and CHENG, C.Z., Phys. Fluids B **2** (1990) 985
[9] ZONCA, F. and CHEN, L., Phys. Fluids B **5** (1993) 3668
[10] CHEN, L., Phys. Plasmas **1** (1994) 1519
[11] SHARAPOV, S.E., *et al.,* Phys. Plasmas **9** (2002) 2027
[12] BREIZMAN, B.N., Phys. Plasmas **10** (2003) 3649
[13] HEIDBRINK, W.W., Phys. Plasmas **15** (2008) 055501
[14] ZONCA, F. and CHEN, L., Plasma Phys. Control. Fusion **48** (2006) 537 (2006)

[15] ZONCA, F., *et al.,* Plasma Phys. Control. Fusion **48** (2006) B15
[16] PARK, W., *et al.,* Phys. Fluids B **4** (1992) 2033
[17] CHENG, C.Z., Phys. Rep. **211** (1992) 1
[18] FU, G.Y., *et al.,* Phys. Fluids B **5** (1993) 4040
[19] ZHENG, L.-J., *et al.,* Phys. Plasmas **7** (2000) 2469
[20] KRAMER, G.J., *et al.*, Phys. Plasmas **13** (2006) 056104
[21] CANDY, J. and WALTZ, R.E., J. Comput. Phys. **186** (2003) 545
[22] CANDY, J., and WALTZ, R.E., Phys. Rev. Lett. **91** (2003) 045001
[23] BREIZMAN, B.N., *et al.,* Phys. Plasmas **4** (1997) 1559
[24] GORELENKOV, N.N., *et al.*, Phys. Plasmas **6** (1999) 629
[25] WALTZ, R.E., *et al.,* Nucl. Fusion **45** (2005) 741
[26] WALTZ, R.E., *et al.,* Phys. Plasmas **14** (2007) 0056116
[27] ESTRADA-MILA, C., *et al.,* Phys. Plasmas **13** (2006) 112303
[28] HAUFF, T. and JENKO, F., Phys. Plasmas **15** (2008) 112307
[29] ANGIONI, C. and PEETERS, A.G., Phys. Plasmas **15** (2008) 052307
[30] ZHANG, W., *et al.,* Phys. Rev. Lett. **101** (2008) 095001
[31] ALBERGANTE, M., *et al.,* Phys. Plasmas **16** (2009) 112301
[32] WALTZ, R.E., *et al.,* Phys. Plasmas **1** (1994) 2229
[33] CANDY, J., Phys. Plasmas **12** (2005) 072307
[34] CONNOR, J.W., *et al.,* Phys. Rev. Lett. **40** (1978) 396
[35] WALTZ, R.E., Phys. Plasmas **17** (2010) 072501
[36] HERNANDEZ. V., *et al.,* ACM Trans. Math. Software **31** (2005) 351
[37] BALAY, S., *et al.,* PETSc Web page, 2009, http://www.mcs.anl.gov/petsc
[38] BALAY, S., *et al.,* PETSc Users Manual, ANL-95/11, Revision 2.3.3, Argonne National Laboratory, 2008
[39] BALAY, S., *et al.,* Modern Software Tools in Scientific Computing (Birkhäuser Press, 1997), pp. 163–202
[40] KAMMERER, M., *et al.,* Phys. Plasmas **15** (2008) 052102
[41] WALTZ, R.E., *et al.,* Phys. Plasmas **13** (2006) 072304